Absolute EUV reflectivity measurements using a broadband high-harmonic source and an *in situ* single exposure reference scheme

JOHANN J. ABEL,[1,*] FELIX WIESNER,[1] JAN NATHANAEL,[1,2] JULIUS REINHARD,[1,2] MARTIN WÜNSCHE,[1,2] GABRIELE SCHMIDL,[3] ANNETT GAWLIK,[3] UWE HÜBNER,[3] JONATHAN PLENTZ,[3] CHRISTIAN RÖDEL,[4] GERHARD G. PAULUS,[1,2] AND SILVIO FUCHS[1,2]

[1]*Institute of Optics and Quantum Electronics, Friedrich Schiller University Jena, Jena, Germany*
[2]*Helmholtz Institute Jena, Jena, Germany*
[3]*Leibniz Institute of Photonic Technology (IPHT), Jena, Germany*
[4]*Institute of Nuclear Physics, Technical University of Darmstadt, Darmstadt, Germany*
[*]*johann-jakob.abel@uni-jena.de*

Abstract: We present a tabletop setup for extreme ultraviolet (EUV) reflection spectroscopy in the spectral range from 40 to 100 eV by using high-harmonic radiation. The simultaneous measurements of reference and sample spectra with high energy resolution provide precise and robust absolute reflectivity measurements, even when operating with spectrally fluctuating EUV sources. The stability and sensitivity of EUV reflectivity measurements are crucial factors for many applications in attosecond science, EUV spectroscopy, and nano-scale tomography. We show that the accuracy and stability of our *in situ* referencing scheme are almost one order of magnitude better in comparison to subsequent reference measurements. We demonstrate the performance of the setup by reflective near-edge x-ray absorption fine structure measurements of the aluminum $L_{2/3}$ absorption edge in α-Al_2O_3 and compare the results to synchrotron measurements.

1. Introduction

Extreme ultraviolet (EUV) and soft x-ray spectroscopy provides a wide range of physical and chemical information on samples. In contrast to visible light, EUV and soft x-ray light interacts with the inner-shell electronic structure of matter providing unique elemental contrast. In addition, the short wavelength of the radiation (1-100 nm) can provide nano-scale resolution in imaging applications [1]. Following the development of laser-driven broadband EUV sources based on high-harmonic generation (HHG) [2] and laser-produced plasmas (LPP) [3] in the past decades, some of the EUV and soft x-ray measurement techniques and applications, that previously were only available at synchrotrons, now can also be performed with these new laboratory-scale light sources. Prominent examples are the investigation of the near-edge x-ray absorption fine structure (NEXAFS) [4,5], photoelectron spectroscopy [6], coherent diffraction imaging [7], novel broadband imaging schemes like XUV Coherence Tomography (XCT) [8,9], or multi-spectral ptychography [10,11].

Moreover, the unique temporal coherence properties of the EUV light from HHG sources support temporal pulse lengths down to the attosecond scale, which opened up a new field of ultrafast research [12–16] by adding the possibility of time resolution to the above-mentioned applications.

However, the stability of laser-based EUV sources is limited due to the highly nonlinear dependence on the driving laser's power or fluctuations in the nonlinear medium or plasma. These fluctuations lead to a reduced sensitivity and inferior detection limits in the above-mentioned methods, which is especially problematic for typically small ultrafast transient effects. Therefore, a major experimental challenge in ultrafast imaging and spectroscopy is the improvement of the stability and sensitivity of the HHG-driven setups [17] e.g. by novel referencing techniques. Several methods have recently been presented to overcome this issue [17–21]. We will categorize these as *in situ* and *ex situ* methods. An *ex situ* reference spectrum can always be recorded by repeating the measurement under the same conditions without the sample or with a reference sample. However, changes in the source spectrum in between these two consecutive measurements cannot be compensated and will thus limit the accuracy of the experiment. *In situ* approaches can overcome this limitation by a direct and simultaneous measurement of the reference. For example, a grating can be used to split the incident EUV beam allowing a simultaneous measurement of a reference signal [19]. It is also possible to merely log the driving-laser parameters during the exposure of the EUV diagnostics and to use a model for the HHG process for extracting the noise [20]. Another additional option is the use of lock-in techniques to increase the detection limit for induced transient effects [21].

In this work, we present an *in situ* referencing approach, which is particularly well-suited for measurements in reflection geometry. Both, the actual measurement and the reference are recorded simultaneously on the same detector. Our method is based on amplitude splitting within the Rayleigh length of a focused EUV beam right in front of the sample under investigation. This is realized by a thin Si_3N_4 membrane, which is placed in close proximity and parallel to the sample's surface. In comparison to *ex situ* reference schemes, the simultaneous measurement of the reference and the sample reflectivity signal with a single EUV spectrometer strongly increases the stability and thus the sensitivity even for single exposure measurements without applying statistics.

In the following, the experimental setup is presented and details of the measurement technique as well as a characterization of the beam-splitting membrane are given. We demonstrate the capabilities of our setup by a reflective near-edge x-ray absorption fine structure (NEXAFS) measurement of sapphire and compare it to synchrotron-based measurements of the same sample. Then, the suppression of source fluctuations of the new method is quantified and compared to an *ex situ* approach. Finally, we discuss the presented method and compare it to previously reported solutions.

2. Experimental setup

The measurements for this work have been carried out at a laser-driven EUV beamline, originally developed for nano-scale cross-sectional imaging [22]. The beamline consists of an HHG source and a toroidal mirror to focus the broadband EUV radiation onto a sample. Subsequently, the reflected light is analyzed with an EUV spectrometer [23]. The high-harmonic generation process is driven by near-infrared (NIR) laser pulses from an optical parametric amplifier (OPA) with $\sim 2\,mJ$ pulse energy, 1 kHz repetition rate, and a pulse duration of $\sim 60\,fs$. The laser radiation is focused with a 30-cm focal length lens into an argon gas jet to produce the high harmonics. In order to generate a quasi-supercontinuous spectrum for broadband reflectivity measurements in the range between 40 and 100 eV, the OPA output wavelength is scanned rapidly between 1250 and 1330 nm [24]. In this way, the strongly modulated harmonic comb is smoothed within the exposure time (typically 5 to 60 seconds) of the EUV spectrometer's CCD and a sufficiently flat broadband EUV spectrum is obtained. Residual NIR light is removed by thin metal filters. Aluminum filters are used for the spectral range from 40 to 72 eV and zirconium filters for the energy region above. Thus, two exposures are needed in order to cover the full spectral range.

As sketched in Fig. 1 the EUV radiation is focused by a toroidal mirror with a focal length of 1 m and illuminates a spot of about 50 μm diameter (FWHM) on the sample under the steep angle of incidence of 15°. The specular reflection is analyzed with an imaging reflection-grating EUV spectrometer (Indigo Optical Systems GmbH). A cylindrical mirror (CM) images the focal point from the sample in the non-dispersive plane directly onto a back-illuminated CCD detector with 13.5 μm pixel size (Andor Newton DO-940). Our self-developed spectrometer features a high spectral resolution of better than 0.08 eV over the entire spectral range and allows to detect even small and sharp spectral features [23].
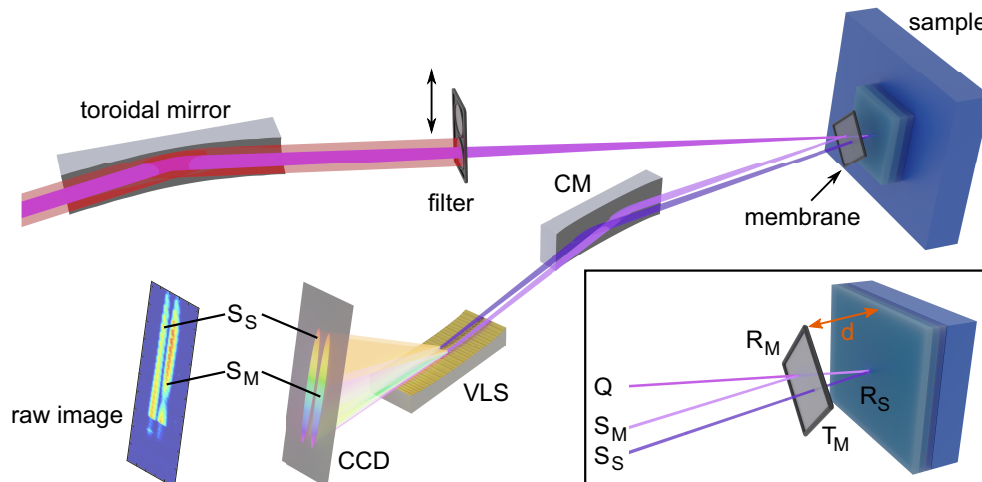

Fig. 1. Sketch of the setup for measuring the absolute reflectivity of samples. Broadband EUV radiation from a HHG source is focused with a toroidal mirror onto the sample under investigation, while remaining laser radiation is eliminated by thin metal filters. Amplitude splitting of the focused beam is realized by a 20 nm thin Si_3N_4 membrane parallel to and in front of the sample's surface. Specular reflection from the membrane (S_M) serves as a reference and is recorded simultaneously with the sample reflection (S_S) by the imaging EUV spectrometer, which consists of a cylindrical mirror (CM), a variable line spacing grating (VLS) and a CCD detector [23].

So far, the absolute calibration of the measured reflectivity has been achieved by an *ex situ* measurement of the source spectrum using an additional reference sample of known reflectance, e.g. TiO_2. In this way, long-term fluctuations of the EUV output power and spectral shape can be mitigated, but short-term effects occurring between subsequent exposures of the reference sample and the actual sample, cannot be accounted for. The *in situ* reference technique presented here complements the beamline by a commercially available 20 nm thin membrane (low-stress Si_3N_4 single window from Norcada Inc.) directly in front of the sample's surface (see Fig. 1). The membrane has a square aperture of 500 μm^2. It acts as a beam splitter within the Rayleigh range of the EUV focus and, accordingly, needs to be placed at a distance of $d \approx 500\,\mu m$ parallel to the surface of the sample.

This approach has two major advantages. First, in contrast to beam splitting in the unfocused EUV beam, the lateral dimensions of the membrane can be limited to a few hundred micrometers. On this scale, very thin (few tens of nanometers) Si_3N_4 membranes can be produced, which improve the overall transmission. Additionally, the wavefront distortions of the reflected beam are minimized, since the membranes are sufficiently flat across the lateral dimensions of the focus. Second, since both reflections propagate collinearly, the splitting geometry allows to measure both, the reflected signal of the membrane and the reflected signal of the sample (which

is transmitted through the same membrane again), simultaneously and with the same camera. However, depending on the divergence, both beams may overlap laterally. Thus, the diagnostic needs to be able to separate the two reflections. In contrast to the commonly used variable line space (VLS) grating flat-field spectroscopic approach, our spectrometer features an additional cylindrical mirror in front of the grating to image the focal points of the sample and the membrane also in the non-dispersive plane onto the CCD detector. Due to the angle of incidence and the distance between membrane and sample, both focal points are imaged onto slightly different positions and thus are spatially separated on the detector. A typical raw image of the separated spectra is shown in Fig. 1. The separation d as well as the angle are controlled by motorized alignment under vacuum conditions.

Accordingly, two spectra are measured at the same time within one exposure of the camera. The reflection of the membrane (S_M) serves as a reference, while the other beam (S_S) carries the reflectivity of the sample (R_S) diluted by two membrane transmissions (T_M^2) (see also inset of Fig. 1). Both signals can be equated by

$$S_M(\omega) = Q(\omega, t) \cdot R_M(\omega) \cdot \eta(\omega) \tag{1}$$

$$S_S(\omega) = Q(\omega, t) \cdot T_M(\omega)^2 \cdot R_S(\omega) \cdot \eta(\omega), \tag{2}$$

where $Q(\omega, t)$ denotes the unknown source spectrum, $R_M(\omega)$ the membrane reflectivity and $\eta(\omega)$ the overall spectrometer efficiency. By using Eqs. (1) and (2), one finds that the unknown sample reflectivity can be extracted,

$$R_S(\omega) = \frac{R_M(\omega)}{T_M(\omega)^2} \cdot \frac{S_S(\omega)}{S_M(\omega)} =: \xi(\omega) \cdot \frac{S_S(\omega)}{S_M(\omega)}. \tag{3}$$

The result is entirely independent of the momentary source spectrum $Q(\omega, t)$. Of course, the membrane-dependent function $\xi(\omega) = R_M(\omega)/T_M(\omega)^2$ needs to be determined, however only once for any given membrane.

3. Results

As a first demonstration of our approach, we present a reflective NEXAFS measurement of an α-Al_2O_3 substrate and compare the results to data recorded at a synchrotron. Since, as described above, the characterization of the membrane is a necessary step to allow absolute reflectivity measurements, we begin with the description of the membrane characterization procedure (chapter 3.1) followed by the actual NEXAFS measurement (chapter 3.2). Finally, in chapter 3.3, the influence of EUV source fluctuations using the new *in situ* approach is analyzed quantitatively and compared to an *ex situ* measurement.

3.1. Membrane characterization

Whereas a separate determination of both membrane properties, reflectivity $R_M(\omega)$ and the transmission $T_M(\omega)$, would be complicated, the required term $\xi(\omega) = R_M(\omega)/T_M(\omega)^2$ can be measured in a simple way. To this end, an inert TiO_2-substrate is used as a reference sample. Its reflectivity, which is depicted in Fig. 2 (b) was measured before at a synchrotron. By evaluating the reflected spectra of the membrane (S_M) and the TiO_2 sample (S_{TiO_2}), the ratio $\xi(\omega)$ can directly be computed:

$$\xi(\omega) = \frac{R_M(\omega)}{T_M(\omega)^2} = \frac{S_M(\omega)}{S_{TiO_2}(\omega)} \cdot R_{TiO_2}(\omega), \tag{4}$$

where $R_{TiO_2}(\omega)$ is the known reflectivity of TiO_2 at 15° angle of incidence.

All results within this work were obtained using Si_3N_4 membranes with a thickness of 20 nm, which were placed $\sim 520\,\mu$m in front of and parallel to the surface of the sample. This
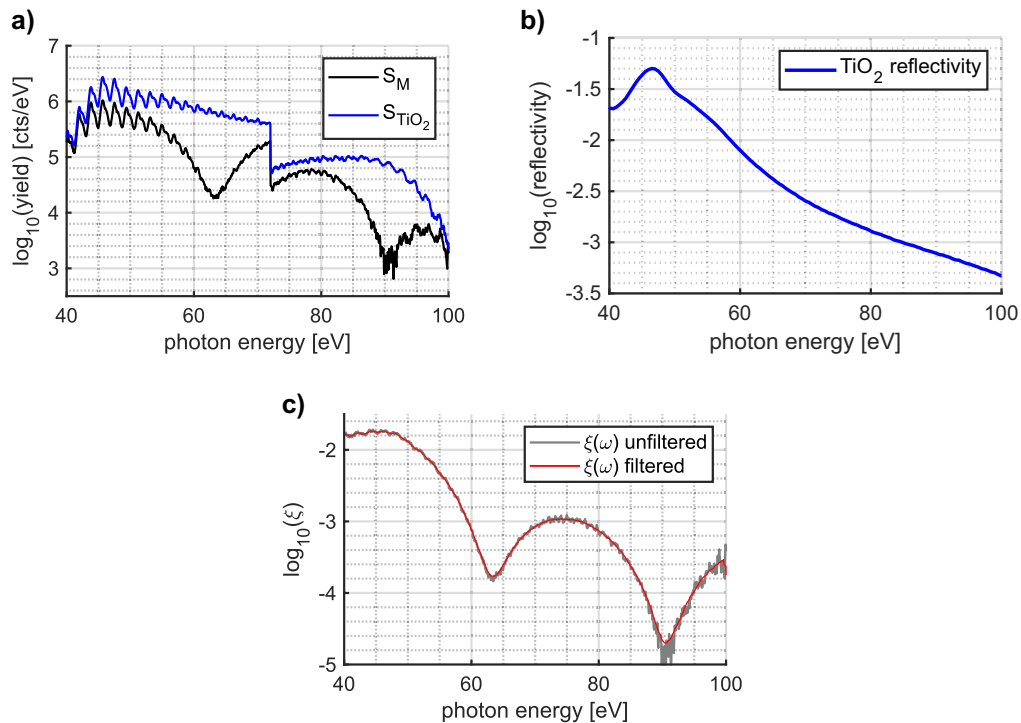
Fig. 2. Characterization of the Si_3N_4 membrane: a) Measured raw data of the spectra reflected from the membrane (black) and the TiO_2 reference substrate (blue) are displayed. The jump at 72 eV arises due to the combination of two recorded exposures using Al and Zr for filtering. b) The reflectivity of the TiO_2 reference substrate has been measured at an angle of incidence of $15°$ at a synchrotron using s-polarized radiation. c) The resulting membrane-dependent ratio $\xi(\omega) = R_M/T_M^2$ is shown before (grey) and after Savitzky-Golay filtering in the wavelength domain (order = 1, width = 0.55 nm) (red). The sine-like curve arises from interference between reflections at the front- and backside of the 20 nm thick membrane.

distance results in $\sim 270\,\mu m$ spatial separation of both reflexes on the spectrometer's CCD, which corresponds to approx. 20 pixels (pixel size $13.5\,\mu m$). A typical raw image of the camera which includes both spectra (membrane and sample reflection) is shown within Fig. 1.

All used membranes were characterized using the same TiO_2 reference and the following data evaluation procedure. At first, the image is rotated to align its axis to the dispersive plane of the grating. Minor sheering effects in the recorded spectra, which are caused by beam pointing shifts during the wavelength scan of the OPA and aberrations of the cylindrical mirror, are accounted for numerically (see Supplement 1). That includes the spatial alignment of each pixel row using the aluminum filter absorption edge for reference. Then, the detector counts are integrated perpendicular to the dispersive axis over 7 pixels for each of the two spectra. Both spectra are weighted by the spectral width of each of the 2048 energy bins. The regions of integration are chosen to always cover a maximum of the recorded intensity while ensuring a complete separation of both spectra. The spectral axis is calibrated by the known peak positions of the high harmonic comb structure from an additional exposure with a fixed wavelength (1300 nm) of the driving laser. To access the full spectral width, two images using an Al- and a NNNQZr-filter have been recorded with an exposure time of 540 s each. Subsequently, the spectra calculated from these images are stitched together.

The resulting signals (integrated counts per eV on the CCD) are shown in Fig. 2 (a). The blue curve represents the reflected signal from the TiO_2 reference substrate while the black one shows the membrane reflection. While the overall trend is rather monotonous for the TiO_2 reflection, the membrane signal exhibits a strong low-frequency spectral modulation. It is caused by interference of EUV radiation reflected from the front and backside of the membrane. This can be understood in perfect analogy to an etalon and can even be used, for example, to measure the thickness of the membrane [25].

Both signals exhibit minor high-frequency modulations. They are caused by the residual high-harmonic comb structure of the source spectrum, which cannot be completely smoothed by the wavelength-scanning method [24]. The discontinuity at ∼ 72 eV is a consequence of stitching the spectra from the two exposures with the two different filters together. Without the *in situ* reference, the spectral transmission curves of the filters would need to be carefully measured, which, in fact, is hardly possible with satisfactory accuracy due to source fluctuations and filter degradation over time.

Finally, the sought-after membrane-dependent ratio $\xi(\omega)$ can directly be calculated from both reflected signals and is depicted in Fig. 2 (c). The modulations caused by the source are entirely canceled out by the division of the two measured spectra. Furthermore, the jump at the stitching point is eliminated. Indeed, since the ratio $\xi(\omega)$ only depends on the Si_3N_4 membrane reflectivity and transmission, it should not exhibit any sharp features or a high-frequency spectral modulations between 40 and 100 eV. Therefore, the extracted ratio $\xi(\omega)$ can further be smoothed using Savitzky-Golay polynomial filtering [26] to reduce noise (red curve).

3.2.　Reflective NEXAFS on α-Al_2O_3

By using the retrieved membrane function $\xi(\omega)$ from the characterization measurement on a TiO_2 sample, the NEXAFS signatures incorporated in the spectral reflectivity of an α-Al_2O_3 substrate have been investigated. The measurement and data evaluation up to the point where the two reflected spectra of the membrane and the sample are retrieved, is equal to the procedure described in the previous chapter. According to Eq. (3) the absolute spectral reflectivity of the sample can be calculated by the division of both recorded spectra weighted by the membrane ratio $\xi(\omega)$. Again, to cover the full spectral width, two exposures each 540 s using Al and Zr filters have been carried out. The spectral range covers a broad region around the $L_{2/3}$-edge of aluminum and thus enables a detailed analysis of the corresponding NEXAFS features.

Figure 3 (a) displays the recorded raw spectra of the α-Al_2O_3 substrate and the membrane at 15° angle of incidence. The spectrum reflected by the membrane (black) again shows the low-frequency spectral modulation. The signal of the Al_2O_3-substrate (blue) is monotonous except for two intense peaks of high reflectivity around 78 eV. The retrieved absolute reflectivity of the sample is shown as a blue line in Fig. 3 (b). For comparison, the green curve shows the retrieved reflectivity of the sample without using the membrane signal, i.e. in a conventional *ex situ* approach, where the source spectrum has been characterized in a prior measurement. Here, the advantages of the new *in situ* approach become obvious as the spectral modulations caused by source fluctuations are efficiently canceled out. The red curve was recorded in a subsequent measurement at the PTB EUV beamline at the "Metrology Light Source" (MLS) in Berlin [27] and serves as a benchmark. One hour of synchrotron beam time was used for the measurement of the reflectivity at 341 monochromatic energies. The energy sampling interval was $\Delta E = 0.1$ eV in the range from 70 to 90 eV and $\Delta E = 0.5$ eV elsewhere.

For a detailed evaluation of the NEXAFS signatures, the same curves are shown again in Fig. 3 (c) in a smaller spectral range. To further reduce high-frequency noise in the laser-based measurements, the reflectivity in the regions excluding the strong peaks between 77.8 eV and 79.2 eV can be smoothed by another Savitzky-Golay filter in the wavelength domain (order = 1,
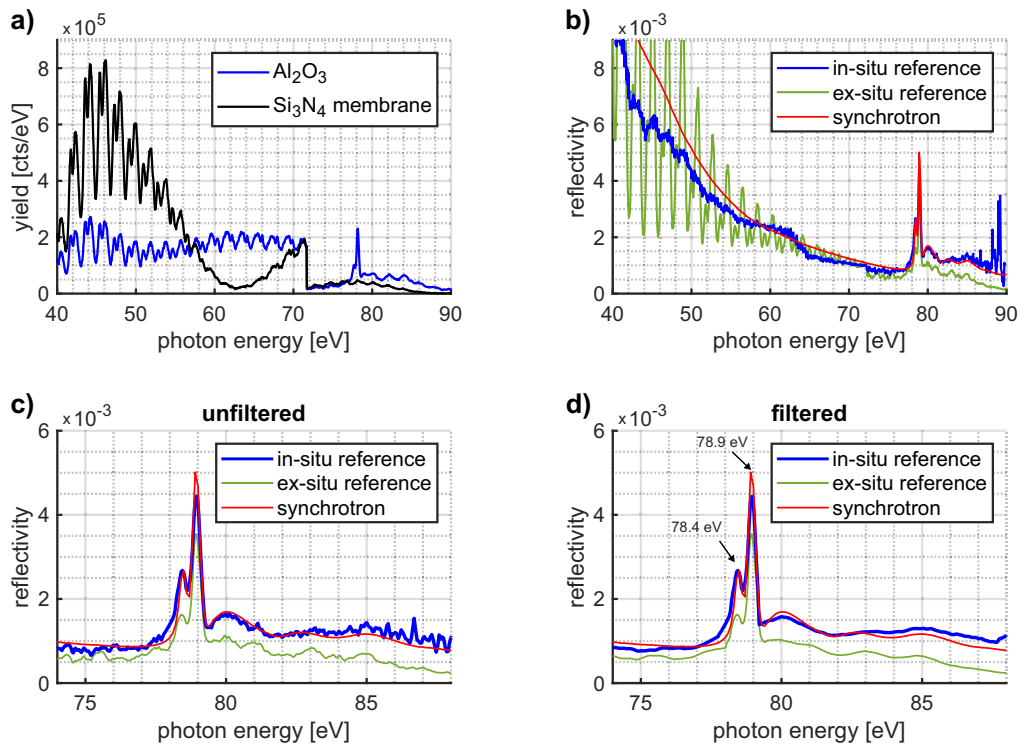
Fig. 3. Broadband reflection measurements at an α-Al_2O_3 substrate. a) The reflected raw spectra from the Al_2O_3 substrate (blue) and the membrane (black) are depicted. Even without elimination of the imperfections of the source spectrum, a prominent spectral structure around 80 eV can be recognized in the Al_2O_3 spectrum, i.e. the NEXAFS feature. b) The retrieved Al_2O_3 reflectivity curve (blue) using the membrane reflection for an *in situ* reference measurement closely follows the reflection data measured at the PTB EUV beamline at the 'Metrology Light Source' (MLS). The laser-based reflectivity data using the conventional *ex situ* reference measurement of a known TiO_2 substrate (green) exhibit large fluctuations at low energies and underestimate the reflectivity above 78 eV. This is strong evidence for variations in the source spectrum between its measurement and the measurement of the reflectivity of the sample. c) Enlarged plot of the reflection spectrum around the aluminum $L_{2/3}$-edge. A clearly resolved double peak structure with maxima at 78.4 and 78.9 eV indicates the splitting of the aluminum L_2 and L_3 edges. d) Additional Savitzky-Golay filtering of the laser-based data reduces noise. In addition, the post-edge structure with additional modulations is visible.

width = 0.19 nm) since no sharp spectral features are expected. The filtered signals are depicted in Fig. 3 (d).

As compared to synchrotron data, the measured reflectivity using HHG radiation shows a very good agreement above energies of 55 eV. The deviation for lower energies most likely originates from the following three measurement uncertainties. Firstly, the aperture tolerance in our instrument implies an uncertainty of the angle of incidence of about one degree. The influence on the measurement is increased since the angle affects both, the measurement of the membrane function $\xi(\omega)$ and the sample reflectivity. Furthermore, we rely on the known reflectivity of the TiO_2 reference for the membrane characterization. The TiO_2 reflectivity has been quantified at the synchrotron as well (see Fig. 2 (b)).

Nevertheless, all three reflection curves show a similar trend in general. Above 70 eV, the measurements with *in situ* reference agree very well with the benchmark curve from the synchrotron, while the spectrum using an *ex situ* reference (green) underestimates the reflectivity by 30 to 50 % and the double peak structure is not fully resolved. The internal structure of NEXAFS features in the energy range from 70 to 88 eV is completely reconstructed using the presented *in situ* measurement scheme and allows the investigation of the spectral fine structure in detail as shown in Fig. 3 (d). However, a small deviation of relative peak amplitudes between synchrotron and laser-based measurements occurs. This is caused by the finite resolution of our spectrometer, which is estimated to be $\sim$ 160 meV in this experiment and thus leads to a reduction of the peak heights. Additionally, the finite discretization of the synchrotron data, which is way more coarse than the spectral resolution of the monochromator can also cause peak height deviations depending on the sampling discretization, especially at sharp spectral variations of the reflectivity (see Supplement 1 for details).

Our measurements confirm the NEXAFS feature in α-Al_2O_3 around 80 eV. The two peaks located at 78.4 eV and 78.9 eV indicate a 0.5-eV split of the L_3 and L_2 edges due to spin orbit coupling, where the 2p core level splits into the $2p_{3/2}$ and $2p_{1/2}$ states. The sharp and narrow spectral structures can be explained by the formation of core excitons [28]. In addition, a characteristic post edge structure with three additional maxima (80.0 eV, 82.7 eV, and 85.0 eV) is observed, which matches very well to data from [29,30].

It is remarkable that the absolute reflectivity measurement by our setup with only two single exposures yield quantitative information comparable to extensive synchrotron measurements, where the reflectivity was quantified for each single photon energy separately. The acquisition of the laser-based measurements took around 20 minutes in total, while the acquisition procedure at the synchrotron lasted around one hour. The NEXAFS spectrum measured with our laser based setup matches also well with earlier synchrotron-based studies using fluorescence yield [30–32] and reflectivity measurements [29]. This holds in terms of peak positions, relative peak amplitudes, spin-orbit splitting, resolution of spin-orbit coupling, and the post-edge structures in accordance to the limitations described above.

3.3. Normalized root-mean-square deviations

In the following section we quantify the stability improvement of the presented *in situ* measurement scheme in comparison to an *ex situ* reference measurement. For this purpose, 49 measurements of the reflectivity of TiO_2 were performed. This series of exposures, i.e. simultaneously recorded reflection spectra from TiO_2 and a Si_3N_4 membrane, is continuously captured with 30 s exposure time each using the transmission window of the Al filter only. In order to calculate the reflectivity, the data processing of the spectra was carried out in the same way as described in chapter 3.2. Since a new membrane was used for this measurement, it was necessary to characterize the membrane-dependent ratio $\xi(\omega)$ following the procedure described in chapter 3.1.

Fluctuations of a data set consisting of n individual values x_i can be characterized using the normalized root-mean-square deviation (NRMSD), which is defined as

$$\text{NRMSD} = \frac{1}{\bar{x}} \sqrt{\frac{1}{n} \sum_{i=1}^{n} (x_i - \bar{x})^2}, \tag{5}$$

where $\bar{x}$ denotes the mean value.

Figure 4 shows the measured reflectivity of TiO_2 based on (a) an *ex situ* reference measurement and (b) our *in situ* approach. The measured reflectivities in the *ex situ* measurements show strong fluctuations due to the fluctuations of the source spectrum, whereas the *in situ* measurement show an impressive improvement of the stability. For quantifying the improvement, the NRMSD of the averaged reflectivity as well as the NRMSD for each photon energy will be determined.
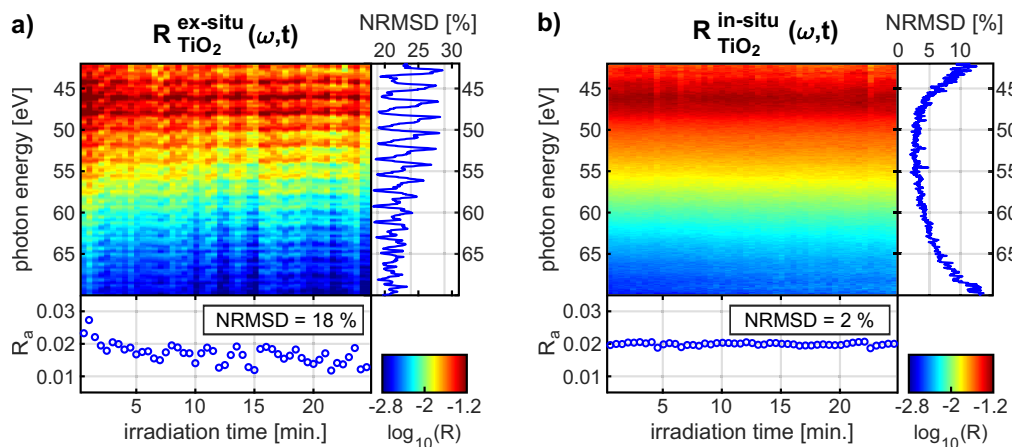

Fig. 4. Measurement of the normalized root-mean-square deviation (NRMSD) for the *ex situ* (left) and *in situ* (right) methods. The reflectivity spectrum of TiO_2 measured in 49 subsequent exposures is shown in false colors. The *ex situ* reference scheme using a separate reference measurement shows pronounced fluctuations, which originate from fluctuations of the EUV source. The averaged reflectivity R_a exhibits an NRMSD of 18 %. (b) *In situ* reflectivity measurements using the Si_3N_4 membrane show a strongly improved stability, quantified by a reduction of the NRMSD to only 2 % for the total reflectivity. Furthermore, the spectrally resolved NRMSDs of the reflectivity values at each energy (blue curves) show a reduction from values between 20 and 30 % to values between 3 and 10 %.

First, the reflectivity is averaged over all energies for each exposure. This averaged reflectivity R_a is plotted as a function of irradiation time below each false color plot of the measured reflectivity. Then, the NRMSD of this signal can be calculated. The *ex situ* measurement shows a NRMSD of 18 %. This error can be directly associated with total EUV intensity fluctuations of the HHG source during the 25 minutes of data accumulation. In contrast the *in situ* measurements only exhibit a NRMSD of 2 %, which can mainly be attributed to remaining detector noise.

Similarly, the NRMSD of the measured reflectivities for each single photon energy are calculated. The corresponding graph is plotted in a sub-graph to the right of Fig. 4 a) and b). While the NRMSD for the *ex situ* data fluctuates between 20 and 30 %, it rarely exceeds 10 % for the *in situ* case, in spectral regions where the signal of membrane reflection is rather low, because of interference effects. In the spectral region from 45 to 65 eV it even remains below 5 %.

4. Discussion

A lab-scale setup for broadband EUV reflectivity measurements based on direct *in situ* reference detection between 40 and 100 eV has been developed, characterized, and tested. Our experimental setup allows for accurate absolute reflectivity determination. Previously observed averaged reflectivity fluctuations in the order of 18 % NRMSD are reduced to only 2 %, while observed deviations of the reflectivity between 20 and 30 % at distinct energies can be restrained to NRMSD values smaller than 10 %.

The presented measurement method using a thin silicon nitride membrane in reflection geometry is perfectly suited to record source fluctuations directly while the radiation is being exposed to the sample. They are eliminated afterwards during the data evaluation. EUV amplitude splitting in the focal region close to the sample is technical demanding but has several significant advantages in comparison to previously reported solutions [17,19–21]. First, we benefit from a direct reference measurement in the EUV and no model or correlation assumption as described in [20] between the optical and EUV is needed. The measurement scheme removes all temporal, spectral and spatial intensity variations of the focused beam. In contrast to beam sampling in the collimated or divergent EUV beam, picking up of the reference in the beam focus requires only a small area of homogeneous, uniform and flat membrane surface, which is a decisive advantage in the EUV.

Our setup employs the full advantage of an imaging spectrometer as the dimension perpendicular to the dispersion direction is exploited. The cylindrical mirror directly images the focal points of the membrane and the sample onto the camera. Therefore, the presented direct reference measurement is independent of the beam divergence and allows even harder focusing. Additionally, the detection scheme uses the same optics (cylindrical mirror, VLS grating) and back illuminated CCD detector for measuring reference and sample spectrum at the same time. Accordingly, the reflection, diffraction and detection efficiencies within the spectrometer are the same and do not influence the measurement, since they cancel out following Eq. (3). In contrast to [19], no additional detector is involved for the simultaneous reference measurement and an extensive cross-correlation characterization between different detectors is not necessary.

The usage of a 20 nm thin Si_3N_4 membrane for the broadband EUV splitting provides an additional important advantage. Its reflectivity is in the order of 10^{-3} and matches very well with typical reflectivity values of investigated samples in the accessible spectral region. Thus, both recorded spectra (sample and reference) have comparable intensities, which allows to benefit from the full dynamic range of the detector.

Numerous ultrafast transient reflectivity measurements with different referencing schemes have been reported [33–37]. Typical exposure times lay in the range of 0.1 s to 3 s [33–35]. However, in order to reach a sensitivity, which allows the detection of transient effects, statistical averaging was always performed. Thus, the total measurement time per time delay in the pump-probe setups was on the order of 10 s to 750 s. The observed transient reflectivity changes reach up to 15 % [34]. With the reported stability of our setup, these effects would be detectable even without any statistical averaging in a single exposure measurements. The required total measurement time is comparable to the existing setups. However we want to point out that we realized the by far steepest incidence angle, which reduces the reflectivity significantly but allows a higher penetration depth. On top of the referencing scheme, the sensitivity of our setup can easily be improved further by statistical averaging.

Clearly, there are also disadvantages with our method. The membrane to sample distance and the resulting separation of both spectra on the detector camera needs to be adjusted precisely. In terms of avoiding beam clipping at the membrane edges, the distance should be minimized. For the further data analysis however, a well defined spatial separation of the spectra on the detector is crucial. This requires appropriate diagnostics and motorization. Furthermore, at distances as close as 500 μm to the sample's surface, there is a certain risk of touching the sample.

As a benchmark of the presented *in situ* reference scheme, we recorded characteristic signatures of the near edge absorption fine structure around the aluminum $L_{2/3}$ edge in α-Al_2O_3 in reflection. The measured absolute reflectivity reproduces the NEXAFS features known from synchrotron data [29,30,32]. Remarkably, the laser-based reflectivity measurement took in total less than 20 minutes, which turns out to be around three times faster than the measurement at the synchrotron. In fact, the measurement time can rather easily be reduced to less than a minute by increasing the HHG flux to the latest state-of-the-art [38].

In the future, we want to extend our setup with a pump beam to enable ultrafast pump-probe measurements and at the same time provide depth information via our EUV coherence tomography approach [9]. Thus, transient effects of encapsulated interfaces can be studied. In addition, our referencing scheme allows for very precise ultra-broadband reflectivity measurements which by itself will increase the accuracy and material-specificity of XCT [39]. In this way, new opportunities for nano-scale spectromicroscopy are created by transferring methods currently confined to synchrotron facilities [40–42] to laboratories.

Disclosures. The authors declare that there are no conflicts of interest related to this article. MW, CR, and SF are shareholders of the Indigo Optical Systems GmbH.

Data availability. Data underlying the results presented in this paper are not publicly available at this time but may be obtained from the authors upon reasonable request.

Supplemental document. See Supplement 1 for supporting content.

References

1. J. Rothhardt, G. K. Tadesse, W. Eschen, and J. Limpert, "Table-top nanoscale coherent imaging with XUV light," J. Opt. **20**(11), 113001 (2018).
2. M. Ferray, A. L'Huillier, X. F. Li, L. A. Lompre, G. Mainfray, and C. Manus, "Multiple-harmonic conversion of 1064 nm radiation in rare gases," J. Phys. B: At., Mol. Opt. Phys. **21**(3), L31–L35 (1988).
3. M. Richardson, "5. Laser Produced Plasmas, in *Vacuum Ultraviolet Spectroscopy I*, vol. 31 of *Experimental Methods in the Physical Sciences* J. Samson and D. Ederer, eds. (Academic, 1998), pp. 83–92.
4. J. Stöhr, *NEXAFS Spectroscopy* (Springer, 1992).
5. C. Peth, F. Barkusky, and K. Mann, "Near-edge x-ray absorption fine structure measurements using a laboratory-scale XUV source," J. Phys. D: Appl. Phys. **41**(10), 105202 (2008).
6. S. Mathias, L. Miaja-Avila, M. M. Murnane, H. Kapteyn, M. Aeschlimann, and M. Bauer, "Angle-resolved photoemission spectroscopy with a femtosecond high harmonic light source using a two-dimensional imaging electron analyzer," Rev. Sci. Instrum. **78**(8), 083105 (2007).
7. H. N. Chapman and K. A. Nugent, "Coherent lensless X-ray imaging," Nat. Photonics **4**(12), 833–839 (2010).
8. S. Fuchs, C. Rödel, A. Blinne, U. Zastrau, M. Wünsche, V. Hilbert, L. Glaser, J. Viefhaus, E. Frumker, P. Corkum, E. Förster, and G. G. Paulus, "Nanometer resolution optical coherence tomography using broad bandwidth XUV and soft x-ray radiation," Sci. Rep. **6**(1), 20658 (2016).
9. S. Fuchs, M. Wünsche, J. Nathanael, J. J. Abel, C. Rödel, J. Biedermann, J. Reinhard, U. Hübner, and G. G. Paulus, "Optical coherence tomography with nanoscale axial resolution using a laser-driven high-harmonic source," Optica **4**(8), 903 (2017).
10. L. Loetgering, X. Liu, A. C. C. De Beurs, M. Du, G. Kuijper, K. S. E. Eikema, and S. Witte, "Tailoring spatial entropy in extreme ultraviolet focused beams for multispectral ptychography," Optica **8**(2), 130 (2021).
11. B. Zhang, D. F. Gardner, M. H. Seaberg, E. R. Shanblatt, C. L. Porter, R. Karl, C. A. Mancuso, H. C. Kapteyn, M. M. Murnane, and D. E. Adams, "Ptychographic hyperspectral spectromicroscopy with an extreme ultraviolet high harmonic comb," Opt. Express **24**(16), 18745 (2016).
12. P. B. Corkum and F. Krausz, "Attosecond science," Nat. Phys. **3**(6), 381–387 (2007).
13. M. Schultze, K. Ramasesha, C. Pemmaraju, S. Sato, D. Whitmore, A. Gandman, J. S. Prell, L. J. Borja, D. Prendergast, K. Yabana, D. M. Neumark, and S. R. Leone, "Attosecond band-gap dynamics in silicon," Science **346**(6215), 1348–1352 (2014).
14. M. Zürch, H.-T. Chang, P. M. Kraus, S. K. Cushing, L. J. Borja, A. Gandman, C. J. Kaplan, M. H. Oh, J. S. Prell, D. Prendergast, C. D. Pemmaraju, D. M. Neumark, and S. R. Leone, "Ultrafast carrier thermalization and trapping in

silicon-germanium alloy probed by extreme ultraviolet transient absorption spectroscopy," Struct. Dyn. **4**(4), 044029 (2017).

15. B. Buades, A. Picón, E. Berger, I. León, N. Di Palo, S. L. Cousin, C. Cocchi, E. Pellegrin, J. H. Martin, S. Manas-Valero, E. Coronado, T. Danz, C. Draxl, M. Uemoto, K. Yabana, M. Schultze, S. Wall, M. Zürch, and J. Biegert, "Attosecond state-resolved carrier motion in quantum materials probed by soft x-ray XANES," Appl. Phys. Rev. **8**(1), 011408 (2021).

16. R. Géneaux, I. Timrov, C. J. Kaplan, A. D. Ross, P. M. Kraus, and S. R. Leone, "Coherent energy exchange between carriers and phonons in peierls-distorted bismuth unveiled by broadband xuv pulses," Phys. Rev. Research **3**(3), 033210 (2021).

17. R. Géneaux, H.-T. Chang, A. M. Schwartzberg, and H. J. B. Marroux, "Source noise suppression in attosecond transient absorption spectroscopy by edge-pixel referencing," Opt. Express **29**(2), 951 (2021).

18. G. D. Lucarelli, B. Moio, G. Inzani, N. Fabris, L. Moscardi, F. Frassetto, L. Poletto, M. Nisoli, and M. Lucchini, "Novel beamline for attosecond transient reflection spectroscopy in a sequential two-foci geometry," Rev. Sci. Instrum. **91**(5), 053002 (2020).

19. K. Yao, F. Willems, C. von Korff Schmising, C. Strüber, P. Hessing, B. Pfau, D. Schick, D. Engel, K. Gerlinger, M. Schneider, and S. Eisebitt, "A tabletop setup for ultrafast helicity-dependent and element-specific absorption spectroscopy and scattering in the extreme ultraviolet spectral range," Rev. Sci. Instrum. **91**(9), 093001 (2020).

20. M. Volkov, J. Pupeikis, C. R. Phillips, F. Schlaepfer, L. Gallmann, and U. Keller, "Reduction of laser-intensity-correlated noise in high-harmonic generation," Opt. Express **27**(6), 7886 (2019).

21. K. Kato, H. Mashiko, Y. Kunihashi, H. Omi, H. Gotoh, and K. Oguri, "Highly sensitive transient reflection measurement in extreme ultraviolet region for tracking carrier and coherent phonon dynamics," Opt. Express **28**(2), 1595 (2020).

22. J. Nathanael, M. Wünsche, S. Fuchs, T. Weber, J. J. Abel, J. Reinhard, F. Wiesner, U. Hübner, S. J. Skruszewicz, G. G. Paulus, and C. Rödel, "Laboratory setup for extreme ultraviolet coherence tomography driven by a high-harmonic source," Rev. Sci. Instrum. **90**(11), 113702 (2019).

23. M. Wünsche, S. Fuchs, T. Weber, J. Nathanael, J. J. Abel, J. Reinhard, F. Wiesner, U. Hübner, S. J. Skruszewicz, G. G. Paulus, and C. Rödel, "A high resolution extreme ultraviolet spectrometer system optimized for harmonic spectroscopy and XUV beam analysis," Rev. Sci. Instrum. **90**(2), 023108 (2019).

24. M. Wünsche, S. Fuchs, S. Aull, J. Nathanael, M. Möller, C. Rödel, and G. G. Paulus, "Quasi-supercontinuum source in the extreme ultraviolet using multiple frequency combs from high-harmonic generation," Opt. Express **25**(6), 6936 (2017).

25. S. Fuchs, A. Blinne, C. Rödel, U. Zastrau, V. Hilbert, M. Wünsche, J. Bierbach, E. Frumker, E. Förster, and G. G. Paulus, "Optical coherence tomography using broad-bandwidth XUV and soft X-ray radiation," Appl. Phys. B **106**(4), 789–795 (2012).

26. A. Savitzky and M. J. E. Golay, "Smoothing and differentiation of data by simplified least squares procedures," Anal. Chem. **36**(8), 1627–1639 (1964).

27. C. Laubis, A. Barboutis, M. Biel, C. Buchholz, B. Dubrau, A. Fischer, A. Hesse, J. Puls, C. Stadelhoff, V. Soltwisch, and F. Scholze, "Status of EUV reflectometry at PTB," Proc. SPIE **8679**, 867921 (2013).

28. C. Sousa, C. de Graaf, and F. Illas, "Core exciton energies of bulk MgO, Al_2O_3, and SiO_2 from explicitly correlated ab initio cluster model calculations," Phys. Rev. B **62**(15), 10013–10021 (2000).

29. W. L. O'Brien, J. Jia, Q.-Y. Dong, T. A. Callcott, J.-E. Rubensson, D. L. Mueller, and D. L. Ederer, "Intermediate coupling in $L_2 - L_3$ core excitons of MgO, Al_2O_3, and SiO_2," Phys. Rev. B **44**, 1013–1018 (1991).

30. C. Weigel, G. Calas, L. Cormier, L. Galoisy, and G. S. Henderson, "High-resolution Al L2, 3-edge x-ray absorption near edge structure spectra of Al-containing crystals and glasses: coordination number and bonding information from edge components," J. Phys. Condens. Matter **20**(13), 135219 (2008).

31. E. O. Filatova and A. S. Konashuk, "Interpretation of the changing the band gap of Al_2O_3 depending on its crystalline form: connection with different local symmetries," J. Phys. Chem. C **119**(35), 20755–20761 (2015).

32. J. M. Chen, J. K. Simons, K. H. Tan, and R. A. Rosenberg, "Correlation between interatomic distances and the x-ray-absorption near-edge structure of single-crystal sapphire," Phys. Rev. B **48**(14), 10047–10051 (1993).

33. J. Husek, A. Cirri, S. Biswas, and L. R. Baker, "Surface electron dynamics in hematite (α-Fe_2O_3): correlation between ultrafast surface electron trapping and small polaron formation," Chem. Sci. **8**(12), 8170–8178 (2017).

34. R. Géneaux, C. J. Kaplan, L. Yue, A. D. Ross, J. E. Baekhøj, P. M. Kraus, H.-T. Chang, A. Guggenmos, M.-Y. Huang, M. Zürch, K. J. Schafer, D. M. Neumark, M. B. Gaarde, and S. R. Leone, "Attosecond time-domain measurement of core-level-exciton decay in magnesium oxide," Phys. Rev. Lett. **124**(20), 207401 (2020).

35. C. Möller, H. Probst, J. Otto, K. Stroh, C. Mahn, S. Steil, V. Moshnyaga, G. M. Jansen, D. Steil, and S. Mathias, "Ultrafast element-resolved magneto-optics using a fiber-laser-driven extreme ultraviolet light source," Rev. Sci. Instrum. **92**(6), 065107 (2021).

36. C. J. Kaplan, P. M. Kraus, A. D. Ross, M. Zürch, S. K. Cushing, M. F. Jager, H.-T. Chang, E. M. Gullikson, D. M. Neumark, and S. R. Leone, "Femtosecond tracking of carrier relaxation in germanium with extreme ultraviolet transient reflectivity," Phys. Rev. B **97**(20), 205202 (2018).

37. M. Lucchini, S. A. Sato, G. D. Lucarelli, B. Moio, G. Inzani, R. Borrego-Varillas, F. Frassetto, L. Poletto, H. Hübener, U. De Giovannini, A. Rubio, and M. Nisoli, "Unravelling the intertwined atomic and bulk nature of localised excitons by attosecond spectroscopy," Nat. Commun. **12**(1), 1021 (2021).

38. R. Klas, W. Eschen, A. Kirsche, J. Rothhardt, and J. Limpert, "Generation of coherent broadband high photon flux continua in the XUV with a sub-two-cycle fiber laser," Opt. Express **28**(5), 6188 (2020).

39. F. Wiesner, M. Wünsche, J. Reinhard, J. J. Abel, J. Nathanael, S. Skruszewicz, C. Rödel, S. Yulin, A. Gawlik, G. Schmidl, U. Hübner, J. Plentz, G. G. Paulus, and S. Fuchs, "Material-specific imaging of nanolayers using extreme ultraviolet coherence tomography," Optica **8**(2), 230 (2021).

40. A. Majhi, M. Nayak, P. C. Pradhan, E. O. Filatova, A. Sokolov, and F. Schäfers, "Soft X-ray reflection spectroscopy for nano-scaled layered structure materials," Sci. Rep. **8**(1), 15724 (2018).

41. A. Pattammattel, R. Tappero, M. Ge, Y. S. Chu, X. Huang, Y. Gao, and H. Yan, "High-sensitivity nanoscale chemical imaging with hard x-ray nano-XANES," Sci. Adv. **6**(37), eabb3615 (2020).

42. D. A. Shapiro, Y.-S. Yu, T. Tyliszczak, J. Cabana, R. Celestre, W. Chao, K. Kaznatcheev, A. L. D. Kilcoyne, F. Maia, S. Marchesini, Y. S. Meng, T. Warwick, L. L. Yang, and H. A. Padmore, "Chemical composition mapping with nanometre resolution by soft X-ray microscopy," Nat. Photonics **8**(10), 765–769 (2014).